Catalysis Today 418 (2023) 114071

Contents lists available at ScienceDirect

Catalysis Today

journal homepage: www.elsevier.com/locate/cattod

Influence of carbon support surface modification on the performance of nickel catalysts in carbon dioxide hydrogenation

Nienke L. Visser [a], Juliette C. Verschoor [a], Luc C.J. Smulders [a], Francesco Mattarozzi [a], David J. Morgan [b], Johannes D. Meeldijk [a], Jessi E.S. van der Hoeven [a], Joseph A. Stewart [c], Bart D. Vandegehuchte [c], Petra E. de Jongh [a,*]

[a] Materials Chemistry and Catalysis, Debye Institute for Nanomaterials Science, Utrecht University, Universiteitsweg 99, 3584 CG Utrecht, the Netherlands
[b] Max Planck-Cardiff Centre on the Fundamentals of Heterogeneous Catalysis FUNCAT, Cardiff Catalysis Institute, School of Chemistry, Cardiff University, Park Place, Cardiff CF10 3AT, United Kingdom
[c] TotalEnergies OneTech Belgium, B-7181 Seneffe, Belgium

ARTICLE INFO

Keywords:
Carbon support
Functionalization
Nickel
CO_2 hydrogenation

ABSTRACT

The interaction between metal nanoparticles and a support is of key importance in catalysis. In this study, we demonstrate that the introduction of oxygen- or nitrogen-containing surface groups on a graphite nanoplatelet support influences the performance of nickel supported catalysts during CO_2 hydrogenation. By careful design of the synthesis conditions, the Ni nanoparticle size of the fresh catalysts was not affected by the type of support surface groups. A combination of H_2 chemisorption and high resolution TEM demonstrates that the available metal surface depends on the interaction with the carbon support. The amination treatment to introduce nitrogen-containing groups results in the weakest interaction between the Ni and the support, showing the highest initial Ni weight-based activity, although at the expense of nanoparticle stability. Hence initial enhancement in activity is not always optimal for long term catalysis. The use of carbon with a higher density of oxygen functional groups that are stable above 350 °C, is beneficial for preventing deactivation due to particle growth. Furthermore, small amounts of contaminants can have a substantial influence on the CH_4 selectivity at low conversions.

1. Introduction

In heterogeneous catalysis, the interaction between (metal) nanoparticles and a support is a crucial factor for the catalytic performance. Stabilizing the nanoparticles is the main reason to use a support, resulting in a high particle dispersion during synthesis [1] and preventing them from sintering during catalysis. In addition, supports can affect the catalytic activity and selectivity, for instance via the absorption of reactants or intermediates, by influencing the particle size or shape, or by altering reaction pathways [2,3].

All mentioned factors can affect the performance of catalysts in the Power-to-Gas process, where CO_2 is hydrogenated to methane. This is a highly interesting reaction to allow the storage of renewable hydrogen in synthetic natural gas [4]. A wide range of metals, for example Ru, Rh and in particular Ni have been investigated for this reaction [5,6]. Compared to noble metals, Ni is relatively low-priced, active and abundant. Typical supports used for this reaction are SiO_2 and Al_2O_3 [6,7], with a recent switch to reducible oxides, such as CeO_2, TiO_2 or ZrO_2 because of their increased CO_2 adsorption activity [8,9]. In this reaction, factors such as metal particle size, support and promoter effects are important to understand, but can at the same time be very challenging to disentangle.

Recently the use of carbon, especially carbon nanotubes (CNTs) as support for CO_2 hydrogenation catalysts has gained more attention for fundamental studies [10–12]. Carbon materials are interesting model supports, because of their relatively high surface area and tunable surface chemistry [13]. Furthermore, carbon supports can be used to diminish the formation of species that strongly interaction with the support, for example metal silicates or aluminates [14–16], or enhance the interaction between active metal and promoters [17].

During methanation, catalyst deactivation is an important factor to consider. This can be caused by the formation of nickel carbonyl species

* Corresponding author.
E-mail address: P.E.deJongh@uu.nl (P.E. de Jongh).

https://doi.org/10.1016/j.cattod.2023.114071
Received 15 December 2022; Received in revised form 16 February 2023; Accepted 26 February 2023
Available online 28 February 2023

at low temperatures, whereas particle growth usually occurs at high temperatures [2,18,19]. Another challenge is the formation of carbon deposits, blocking the active metal surface, although this can be prevented by working at elevated pressures [20]. Carbon offers a high heat conductivity [10], which is crucial to prevent the formation of local hot spots during the exothermic methanation reaction ($\Delta H^o = -165$ kJ mol^{-1}) [21]. Modifying the surface chemistry of a support can help to stabilize nanoparticles.

Typical support surface groups introduced to carbon supports are oxygen and nitrogen containing groups, changing the chemical properties of the carbon surface without changing its structural properties [22–24]. As a result, it is possible to vary the point of zero charge (PZC) and consequently the acidity or basicity over a wide range. A reflux treatment of pristine carbon (in this case graphite nanoplatelets, GNP) in HNO_3 typically results in the incorporation of carboxylic, lactone and anhydride surface groups [25–27], increasing the acidic character of the material. An amination treatment of the oxidized carbon (GNP-O) converts the oxygen- into nitrogen-containing surface groups (GNP-N), which increase the surface basicity [22,23,28]. Support surface groups are often found to influence the final metal particle size of fresh catalysts. They can enhance the wetting of the precursor solution or can anchor the metal precursor more strongly [29]. Both could result in smaller nanoparticles [30–35], or even single atoms or clusters [12,36].

Functionalization of carbon supports can improve the catalyst stability, by preventing nanoparticle growth [37–39]. Besides, the catalytic activity can be modulated, for instance by introducing N-containing species, to increase the basicity of the support [10,21,40–42], allowing enhanced CO_2 adsorption [23]. Gonçalves et al. performed a systematic study on the effect of support surface treatment of nickel on active carbon for low pressure CO_2 hydrogenation and found that the use of the most basic carbons resulted in the highest catalytic activity [40]. However, the interference of differences in nanoparticle size on catalysis and the effect of support modification on catalyst stability were not addressed in full detail.

In this paper, we discuss the effect of support functionalization for high pressure CO_2 hydrogenation using graphite carbon nanoplatelets (GNP) as model support for Ni nanoparticles. Both oxygen and nitrogen containing surface groups were introduced to the carbon support surface before deposition of the nickel. We kept other parameters, such as the initial Ni particle size, the same and discuss the effect of the support treatment on catalytic performance during CO_2 hydrogenation at 300 °C and 30 bar, with main focus on catalyst stability.

2. Experimental

2.1. Synthesis of carbon supported nickel catalysts

Nickel nitrate hexahydrate ($Ni(NO_3)_2{\cdot}6H_2O$, Sigma Aldrich, ≥ 97.0%), nitric acid (HNO_3, Merck, 65%) and Silicon Carbide, (SIKA ABR I, F70) were used as received. Graphite nanoplatelets (GNP-500, XG Sciences, grade C ~500 m^2 g^{-1} surface area) were either used as received, referred to as GNP, functionalized with oxygen-containing support surface groups (GNP-O) or nitrogen-containing support groups (GNP-N) or washed (GNP-W). To prepare oxidized carbon, approximately 10 g of the pristine GNP-500 was heated in 400 mL 65% HNO_3 to 80 °C for 2 h while stirring. Afterwards, the suspension was washed several times with 5 L demi water each time until a pH of 6 was reached. After the last washing step, the support was dried at 120 °C for at least 24 h and subsequently crushed. Nitrogen functionalities were introduced to the support by substitution of oxygen functionalities [43]. Typically, ~3 g GNP-O was loaded into a tubular oven, purged for 15 min with N_2 gas at room temperature (200 mL min^{-1}) and subsequently exposed to a flow of NH_3 gas at 600 °C (220 mL min^{-1}, 5 °C min^{-1}, 4 h). To prepare GNP-W, approximately 2 g GNP was washed in 50 mL 1 M HNO_3 at room temperature while stirring for 2 h. Afterwards the suspension was washed several times with 100 mL demi water each time until a pH of 6 was reached and dried in the same way as GNP-O.

Nickel was deposited on either GNP, GNP-O, GNP-N or GNP-W using incipient wetness impregnation. Typically, 1.0 g of carbon support was dried in a round-bottom flask for 120 min at 170 °C, while stirring under dynamic vacuum to remove water and air from the pores. Aqueous nickel nitrate solutions were prepared by dissolving 2.0 M $Ni(NO_3)_2$ in mili Q water. The solution was acidified with 0.10 M HNO_3 to ensure a pH around 1. The dried carbon support was impregnated with 0.73 mL $g_{support}^{-1}$ (90% of the pore volume of pristine GNP, determined using N_2 physisorption) under static vacuum while stirring, to ensure that the solution was homogeneously spread over the support. Subsequently the sample was dried overnight at room temperature under dynamic vacuum. To decompose the precursor, 1 g of the sample was transferred to a plug-flow reactor and heated to 350 °C in 200 mL min^{-1} N_2 (3 °C min^{-1}, 90 min) to decompose the nitrate. The reactor was then cooled down and the gas was switched to 5% H_2/N_2 (200 mL min^{-1}), which was the gas atmosphere for the subsequent reduction at 350 °C (2 °C min^{-1}, 90 min). After cooling down, the catalyst was slowly exposed to air to passivate the nickel nanoparticles. The catalysts are denoted as Ni/GNP-*X*, where GNP-*X* is the type of carbon used (GNP, GNP-O, GNP-N or GNP-W).

2.2. Structural characterization

The pore volume and surface area of carbon supports were analyzed using N_2-physisorption. Isotherms were measured at − 196 °C on a Micromeritics TriStar II Plus apparatus. The samples were dried overnight under vacuum at 170 °C before the measurement. The specific surface area of the support was calculated using the BET equation ($0.05 < p/p_0 < 0.25$) and the total pore volume was derived from the amount of N_2 adsorbed at $p/p_0 = 0.995$.

The density of acidic and basic surface groups was determined by potentiometric titration using a TIM 880 Titralab Titration Manager. The carbon materials were suspended in 65 mL 0.1 M KCl solution and degassed under N_2 flow and vigorous stirring. For both acid and base titrations ~25 mg of carbon material was used. The titrations were performed with either a 0.01 M NaOH or 0.01 M HCl solution, both in 0.1 M KCl solution. The amount of surface groups per gram carbon material was calculated based on the equivalence points of the titration data. Combined with the BET surface area obtained from physisorption, the density of surface groups (# groups nm^{-2}) was determined for the different supports. The point of zero charge (PZC) of the support was determined through mass titration of the carbon material. Increasing amounts of carbon material were suspended in 10 g of 0.1 KCl solution, increasing the weight percentage of the support in the liquid, while measuring the pH. It is assumed that the amphoteric behavior of the surface groups will lead to a system pH equal to the PZC.[44].

The supports were imaged with scanning electron microscopy (SEM) on a Helios G3 UC at 2 or 5 kV. The images were measured in field-free mode with a current of 0.40 nA. EDX analysis was performed using an Oxford silicon drift detector and Aztec software.

The catalysts were imaged with transmission electron microscopy (TEM) on a Thermo Fisher Talos L120C operated at 120 kV or a Thermo Fisher Talos F200X microscope operated at 200 kV. The catalyst sample was dispersed as a dry catalyst powder onto a Cu sample grid coated with holey carbon (Agar 300 mesh Cu). Because of the nature of the carbon, consisting of thin graphitic sheets, dispersion of the catalyst powder in a solution and subsequent sonication was not necessary during the sample preparation. At least 400 nickel nanoparticles were manually counted per catalyst sample on at least 8 different catalyst locations using ImageJ analysis software. The determination of the Ni particle sizes is described in Supporting Information Section 1.

High resolution TEM imaging was performed on a Thermo Fisher Spectra 300 monochromated, double-aberration corrected microscope operated at 300 kV. High angle annular dark field scanning transmission electron microscopy (HAADF-STEM) and integrated differential phase contrast (iDPC) images were acquired in parallel. The screen current was

ca. 0.05 nA and the camera length 145 mm.

Powder X-ray diffraction (XRD) was performed on a Bruker D2 X-ray diffractometer, equipped with a Co-$K_{a1,2}$ radiation source ($\lambda = 1.790$ Å) and a Lynxeye detector. All catalysts were measured with diffraction angles varying between 10° and 95° 2θ with a step size of 0.05° 2θ/step while the sample was rotated at a rate of 15 rpm. All diffractograms were normalized to the carbon (002) peak at 30.9°. The crystallite sizes were calculated by applying the Scherrer equation to the NiO (111) peak at 43° or the Ni^0 (200) peak at 61°.

Thermogravimetric analysis was performed on a Perkin Elmer TGA800 coupled to an Hiden Analytical HPR-20 MS system. For the bare supports, the weight of 4–8 mg sample was determined while heating in Ar (10 °C min^{-1}) to identify the weight % of functional groups on the supports. This technique was also used to determine the Ni weight-loading of the catalysts before and after catalysis as reported before [45] and described in detail in the Supporting Information Section 1.

A Kratos Axis Ultra DLD system was used to collect XPS spectra using a monochromatic Al Kα X-ray source operating at 168 W (12 mA x 14 kV). Data was collected with pass energies of 160 eV for survey spectra, and 20 eV for the high-resolution scans with step sizes of 1 eV and 0.1 eV respectively. The system was operated in the Hybrid mode, using a combination of magnetic immersion and electrostatic lenses, and acquired over an area of approximately 300 × 700 μm^2. A magnetically confined charge compensation system using low energy electrons was used to minimize charging of the sample surface and all spectra were taken with a 90° take of angle. A pressure of ca. 5 × 10^{-9} Torr was maintained during collection of the spectra. All samples were mounted into recesses of a modified Kratos Axis Ultra standard sample bar and gently pressed flat with iso-propyl alcohol cleaned glass slides before insertion into the spectrometer. All data was analyzed using CasaXPS (v2.3.24) [46] after subtraction of a Shirley background and using modified Wagner sensitivity factors as supplied by the instrument manufacturer. Cure fits were performed using an asymmetric Lorentzian form (LA line shape in CasaXPS), whereas the line shape for graphitic, sp^2 carbon, was based on a cleaved, oxygen free HOPG sample.

Temperature-programmed desorption (TPD) was performed on a Micromeritics AutoChem II 2920 apparatus. For the bare supports, 80 mg support was dried at 120 °C in Ar for 15 min. The sample was cooled down to 40 °C and subsequently heated in Ar (15 mL min^{-1}) with 5 °C min^{-1} to 900 °C. H_2O was captured with a dry ice/isopropanol cold trap. The outgoing gas was analyzed using a mass spectrometer (MS) of Hiden Analytical equipped with a QGA Professional software package.

H_2 chemisorption was measured on a Micromeritics ASAP 2020 C apparatus using ~100 mg of sample. Prior to the measurement, the sample was reduced in pure H_2 (6.0, Linde) at 300 °C for 2 h (5 °C min^{-1}), after which full reduction was assumed, based on TPR analysis. The sample was then evacuated and cooled to 35 °C, and H_2 chemisorption was measured at that temperature. The Ni surface area was obtained from extrapolation of the linear range of the adsorption isotherm of H_2 to a pressure of 0 kPa, giving the H_2 uptake (μmol g_{cat}^{-1}). The determination of the experimental and theoretical Ni surface areas is described in Supporting Information Section 1.

2.3. Catalytic performance testing

The CO_2 methanation catalysis was performed in a high throughput gas-phase 16-parallel fixed bed reactor system (Avantium Flowrence). Prior to the catalytic test, the catalyst powders were pelletized using a hydraulic press and subsequently sieved into a fraction of 75–150 μm. 60 mg catalyst was diluted with 240 mg SiC (>150 μm) to prevent the formation of hotspots. The mixture of catalyst granules and SiC were loaded in stainless steel reactor tubes (2.6 mm inner diameter) on top of ~0.5 cm SiC granules. This was topped off with SiC.

The Ni/GNP-*X* catalysts were *in situ* reduced prior to the reaction in a flow of 10% H_2/N_2 at 300 °C (2 °C min^{-1}) for 3 h. Subsequently the reactors were cooled down to 120 °C before the reaction mixture was added. The reaction mixture consisted of CO_2:H_2:He = 19:76:5, 120 mL min^{-1}, and was divided over 16 reactors. The resulting GHSV was 7500 mL g_{cat}^{-1} h^{-1}. The reactor was gradually pressurized to 30 bar and subsequently heated to 300 °C with 2 °C min^{-1}. This temperature was determined with TPR, see Fig. S1. The catalysts were tested up to 100 h to study both the activity and stability. The products were analyzed directly with online gas chromatography (GC, Agilent 7890B) with a sampling time of 14 min. Thus when all 16 reactors were in use, each sample was analyzed every ~4 h. For each catalyst, three reactors were loaded and tested. After confirming the reproducibility, the catalytic results were averaged.

To test the selectivity at different conversions, after 100 h the GHSV was varied. The total flow over the 16 reactors was adapted (50, 75 and 150 mL min^{-1} total flow) while keeping the gas mixture the same. Each new flow was equilibrated for 1 h and at least 2 datapoints per catalyst were taken (with 4 h difference). After the reaction, the catalysts were flushed with He and left to cool down to 60 °C before exposing them to air. This resulted in controlled passivation for post-catalytic characterization, for which the contents of the three reactors were combined. The formulas to determine the conversion, selectivity and turnover frequency are described in Supporting Information Section 1.

3. Results and discussion

3.1. Effect of functionalization on support properties

Table 1 shows the structural characteristics of the graphite nanoplatelets that were used as-received (pristine, GNP), after the oxidation treatment (GNP-O) and after the amination treatment (GNP-N). The BET surface area and total pore volume of pristine carbon were 456 m^2 g^{-1} and 0.81 mL g^{-1}, respectively. After surface modification, GNP-O and GNP-N exhibited a surface area of to 415 and 308 m^2 g^{-1} and pore volume of 0.72 and 0.62 mL g^{-1}, respectively. The N_2 physisorption isotherms are shown in Fig. S2. A decrease in surface area and pore volume is common for this relatively harsh oxidation treatment [22,47,48] and is probably due to the removal of an amorphous carbon fraction (with high specific surface area) as well as some collapse of the ordered graphite pore structure.

The pristine GNP contained oxygen and its overall surface chemistry was slightly acidic (Table 1, Fig. S3). With the introduction of more oxygen-containing surface groups, the acidity increased, as evidenced by a decrease of the point of zero charge (PZC) from 4.0 to 3.0 (Table 1, Fig. S4). With the introduction of nitrogen functionalities, the PZC was increased to 9.0 and only basic groups were detected with titration (Table 1).

Support treatment did not lead to significant changes in the X-ray diffractograms between 2θ = 20 and 95° (Fig. S5). At lower angles an extra peak was present for GNP, which mostly disappeared upon surface treatment. This likely indicated that the treatment influenced the stacking of the carbon platelets. The D-parameter represents the ratio between sp^2 and sp^3 carbon and is derived from the differential of the carbon x-ray induced Auger peak in the XPS spectrum [49,50]. This value was similar for all carbons (between 21.5 and 22.5 ± 1.0 eV), corresponding to a sp^3 carbon content of ca. 10% [49]. This value was in good agreement with the C1s fitting (Table S1). No significant differences in morphology between the highly graphitic GNP and GNP-O were identified with scanning electron microscopy (SEM) (Fig. S6).

The nature of the oxygen functionalities was investigated by following the gas release of the supports with temperature programmed reduction coupled with mass spectrometry (TPD-MS) up to 900 °C in argon (Fig. 1). We first consider the pristine and oxidized carbon supports. In both cases CO_2 and CO were released, due to the presence of oxygen-containing surface groups. In the case of GNP-O about double the amount was released compared to GNP, in line with the differences in acidity (Table 1). In addition thermographic analysis (TGA) showed a larger weight-loss of GNP-O (9.6%) than GNP (5.4%) at 800 °C in Ar

Table 1
Overview of the physical and chemical properties of the carbon supports.

Support	BET Surface area[a] ($m^2\ g^{-1}$)	Total pore volume[a] ($mL\ g^{-1}$)	Oxygen content[b] (at%)	Nitrogen content[b] (at%)	D- parameter[b] ± 1.0 (eV)	Acidity[c] (# groups nm^{-2})	Basicity[c] (# groups nm^{-2})	PZC
GNP	456	0.81	4.6	-	21.5	0.19	-	4.0
GNP-O	415	0.72	7.7	0.2	22.5	0.81	-	3.0
GNP-N	308	0.62	0.9	2.0	22.5	-	0.17	9.0

Determined with [a] N_2 physisorption, [b] XPS, [c] acid/base titration.

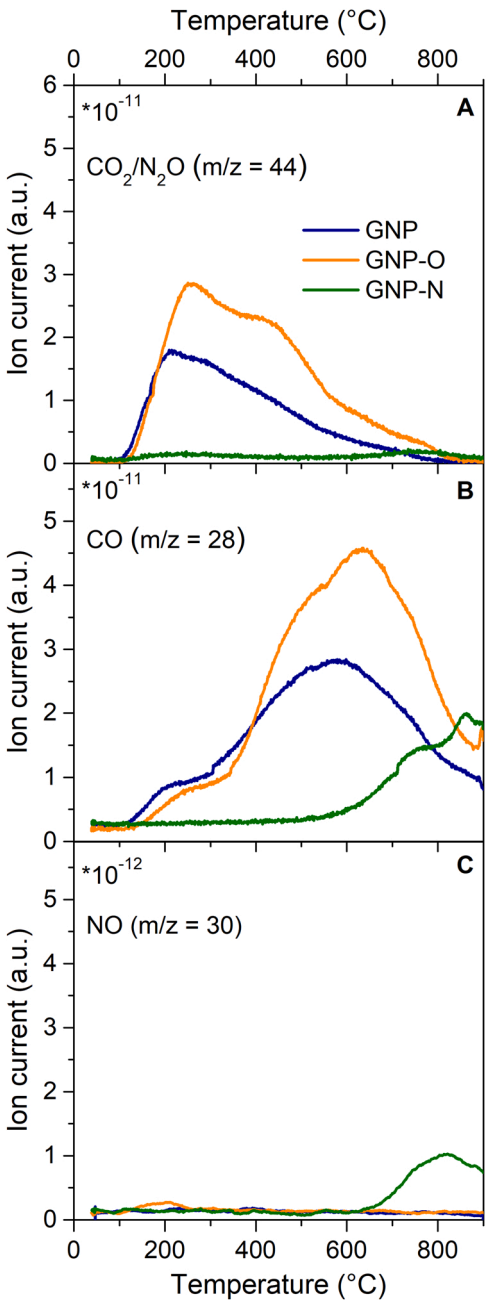

Fig. 1. Release of **(A)** CO_2, **(B)** CO and (**C**) NO as measured with MS while heating three different carbon supports during TPD-MS in argon (5 °C min^{-1}).

(Fig. S7), confirming the presence of more oxygen in the carbon.

The formation of CO_2 (Fig. 1A) was attributed to the decomposition of carboxylic acids (100 and 400 °C), anhydrides (200 – 600 °C) and lactone groups (400 – 900 °C) [25–27,51]. CO formation (Fig. 1B) at low temperatures (< 300 °C) was caused by to the decomposition of aldehyde or ketone groups [25,52]. At higher temperatures, the peaks are typically ascribed to the decomposition of anhydrides (350 – 600 °C), phenols (500 – 750 °C) and carbonyl or quinone groups (650 – 950 °C) [22]. Altogether, TPD-MS analysis showed that the oxidation treatment had resulted in the incorporation of a range of oxygen containing surface groups, that could be carboxylic acids, anhydrides and phenols.

Interestingly, for GNP-N, Fig. 1A and B show that only minor amounts of CO_2 and CO were released; only above 600 °C a peak was observed for $m/z = 28$. This peak could either represent the formation CO from relatively stable oxygen containing surface groups (carbonyls or quinones) or the formation of N_2 from nitrogen containing surface groups. The absence of CO_2 and CO release at lower temperatures indicates that with the amination treatment, (most) oxygen containing surface groups were successfully removed. The release of some NO ($m/z = 30$, Fig. 1C) implies that nitrogen-containing groups had been successfully introduced to the support and that (part of) the nitrogen functional groups also contained oxygen, in agreement with results reported by Arrigo et al. [53].

XPS analysis (Table 1) showed the increase in oxygen content for GNP-O (7.7 at%) with respect to the GNP (4.6 at%). The amination treatment was observed to cause significant loss of oxygen (<1at% left in GNP-N), whilst there was a concomitant increase in nitrogen (2 at%). High resolution spectra analysis of both C1s and N1s regions was performed to understand the chemical functionality. Fitting of the O1s spectra of the GNP materials (Fig. 2A) identified contributions of two major peaks located at ca. 531.5 eV and 533 eV, corresponding to oxygen doubly or singly bound to carbon, respectively,[6,40] whilst the peaks between 535 and 540 eV are characteristic of a shake-up structure for carbonyl containing species.

The oxidation treatment doubled the C═O content (1.4 at% in GNP to 3.0 at% in GNP-O), and also exhibited a corresponding increase in the C−O functionality from 2.3 to 3.5 at% (Table S1), whilst amination caused low levels of these species to remain (0.5 and 0.3 at% for C═O and C−O respectively). The C1s spectra were more complicated to fit given the similar binding energies of some oxygen and nitrogen containing functions, together with the asymmetry of the graphitic carbon and the uncertainty in the shape of the photoelectron background [49]. Nevertheless, XPS confirmed for GNP-O a high amount of several types of oxygen functional groups, with the groups comprising of either a C−O or a C═O bond being dominant over the COO− groups (Fig. S8, Table S1).

The main peak in the XP N1s spectrum of GNP-N is located at ca. 398 eV and is attributed to pyridinic-type groups (Fig. 2B, Table S2), whilst the peak at ca. 400 eV corresponds to pyrrolic- or pyridonic-type nitrogen species [26,53] or absorbed NH_x. The smaller peaks between 402 and 405 eV could originate from graphitic N (~403 eV) and oxidized nitrogen (~405 eV) [54], however given the signal at 398 eV and these higher energy signals, these are likely to be attributed to loss structure from nitrogen in conformations such as that found in g-C_3N_4 [55]. In short, our findings from the XPS analysis and the TPD-MS analysis are in agreement and confirm the presence of oxygen or nitrogen-containing surface groups on the carbon support. Hence with the oxidation and subsequent amination treatment of GNP, three supports were prepared with different acidity/basicity and different types

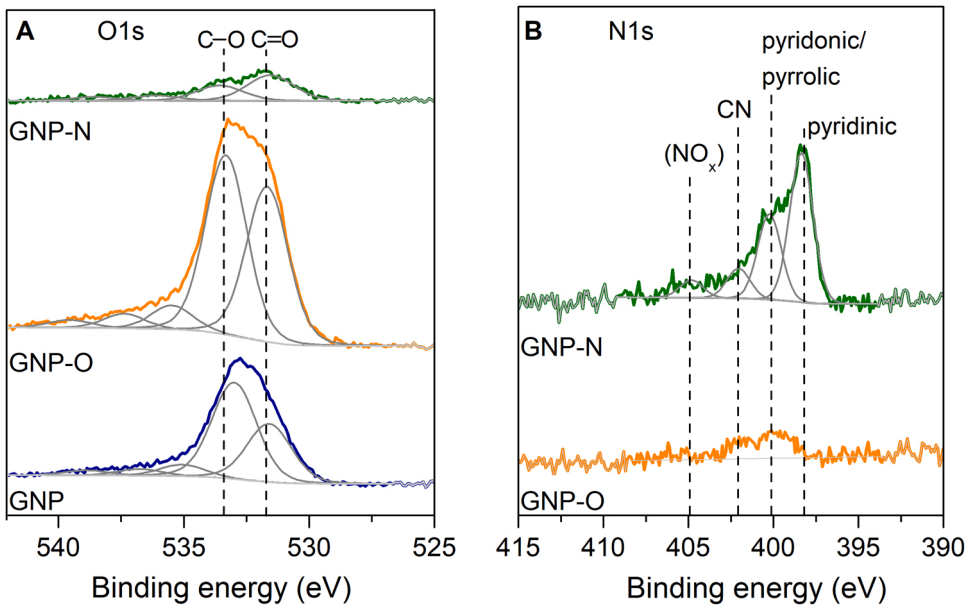

Fig. 2. XP spectra of **(A)** O1s and **(B)** N1s regions of the GNP (blue), GNP-O (orange) and GNP-N (green) supports highlighting different oxygen and nitrogen functionalities.

and amounts of support surface groups; C−O and C═O groups for GNP and GNP-O and mainly pyridinic N for GNP-N.

3.2. Carbon supported Ni catalysts

The main goal was to deposit Ni nanoparticles on the different supports without changing other parameters such as Ni particle size or loading. Indeed, all catalysts contained a Ni loading of ~8 wt% and Ni nanoparticles of about 5 nm in diameter (Table 2). The nickel deposition lowered the BET surface areas, but to a similar extent for all catalysts (249, 238 and 218 m^2 g^{-1} for Ni/GNP, Ni/GNP-O and Ni/GNP-N, respectively, Table S3). The properties for the used catalysts, also displayed in Table 2, will be discussed in detail in Section 3.5.

The D-parameter (Table S4) of the fresh Ni/GNP and Ni/GNP-O catalysts, determined from the Auger peak in XPS, was 22 – 23 ± 1.0 eV, in agreement with ~10% sp^3 carbon determined from the fitting of the C1s spectra (Table S4). Thus, the nickel deposition yielded negligible difference in the graphitic nature of the support. At the elevated temperatures used during Ni deposition (350 °C), carboxylic acid groups were not stable. As a consequence, the ratio between the C−O and C═O groups decreased upon Ni deposition (Fig. S9, Table S5). Hence C═O functionalities were preferentially retained after Ni deposition. This could either mean that these are more stable than C-O containing groups or, less likely, that the Ni nanoparticles bind preferably to C−O surface groups. For the Ni/GNP-N, the presence of nitrogen was evidenced by TGA-MS analysis, as NO_x was released between 300 and 700 °C while heating this catalyst in oxygen atmosphere, which was done to determine the Ni weight loading (Fig. S10).

Fig. 3A-C show transmission electron microscopy (TEM) images of three catalysts prepared using pristine (A, blue), oxidized (B, orange) and aminated (C, green) carbon with corresponding particle size distributions (insets in A, B and C). Independent of the support used, the surface averaged particle diameter (d_s) was 5 nm (Table 2). Although the TEM particle size was similar for all catalysts, the metallic surface area, determined using H_2 chemisorption (Table 2, Table S6 and Fig. S11) was higher for Ni/GNP-N than for Ni/GNP and Ni/GNP-O. The experimental metal surface area of Ni/GNP-N was in agreement with the theoretical surface area calculated from the TEM particle size for a spherical nanoparticle, whereas for the other catalysts clearly lower specific metal surface areas were measured.

The NiO(111) crystallite sizes determined from the peak at 2θ = 43° were 4.2, 5.2 and 3.2 nm for Ni/GNP, Ni/GNP-O and Ni/GNP-N respectively (Fig. 3D, Table 2), roughly matching the TEM results. The peak at low angles and the increased background of the bare GNP had disappeared, indicating that the nickel deposition had caused changes in the morphology of the GNP. No crystalline Ni_3C was observed with XRD. Whilst this is not definitive proof of the absence of Ni_3C, because of the relatively small peak shift compared to Ni, XPS supports this finding. Carbides typically give a distinct and narrow peak or shoulder in the lower binding energy side of the C1s peak (between 282.5 and 283.5 eV)

Table 2
Properties of the fresh and used Ni catalysts on different carbon supports.

Catalyst	Ni wt loading[a] ± 0.4 (wt%)	$d_s \pm \sigma_s$[b] (nm)	Theoretical metal surface area[c] (m^2 g_{Ni}^{-1})	Ni(O) Crystallite size (nm)	Experimental metal surface area (m^2 g_{Ni}^{-1})	TOF[d] ($*10^{-2}$ s^{-1})
Before catalysis (t = 0 h)						
Ni/GNP	8.0	5.3 ± 1.4	13 * 10^1	4.2[e]	86	1.3
Ni/GNP-O	7.8	5.1 ± 1.2	13 * 10^1	5.2[e]	94	1.5
Ni/GNP-N	8.0	5.0 ± 1.7	13 * 10^1	3.2[e]	13 * 10^1	1.6
After catalysis (t = 100 h)						
Ni/GNP	7.7	7.6 ± 2.4	89	5.4 [f]	78	1.1
Ni/GNP-O	8.2	6.0 ± 2.0	12 * 10^1	-	80	1.4
Ni/GNP-N	7.6	10.7 ± 5.6	63	5.6[f]	81	1.6

[a]Determined using TGA-MS, [b] TEM particle diameter, [c] based on TEM particle diameter assuming freestanding spherical particles, [d] derived from H_2 chemisorption, [e] determined from the width of the NiO (111) XRD peak at 2θ = 43°, [f] determined from the width of the Ni (200) XRD peak at 2θ = 61°.

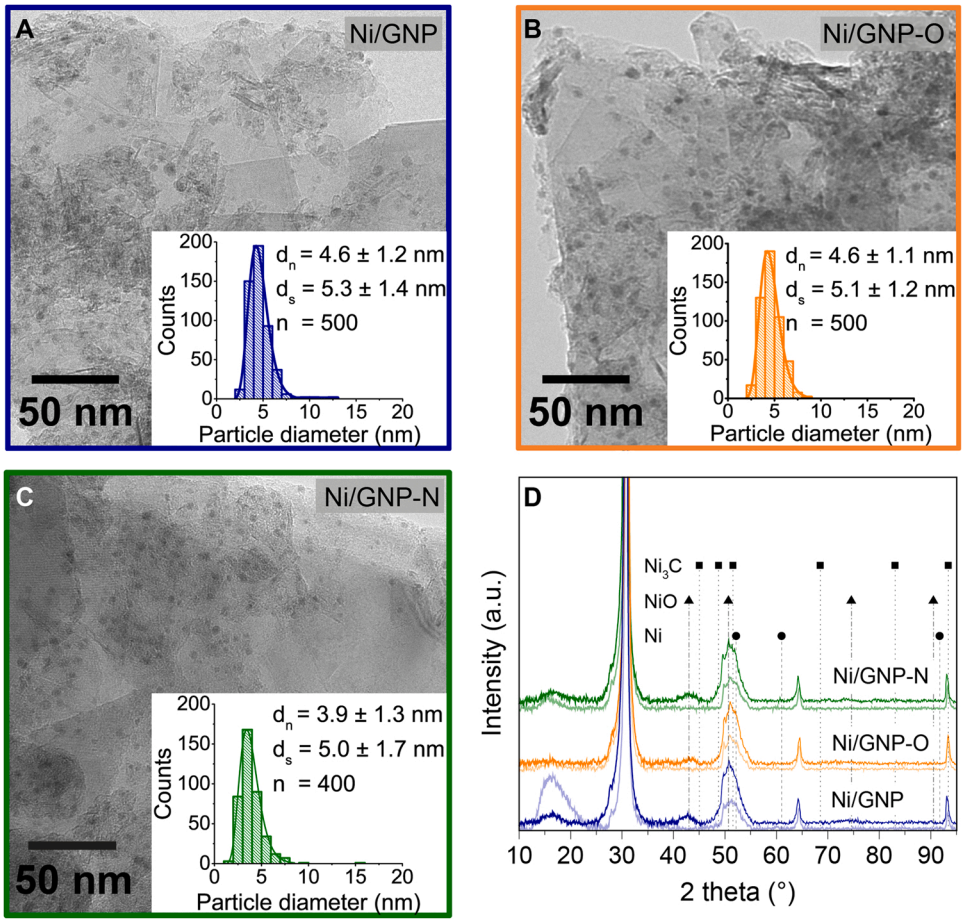

Fig. 3. A-C) Transmission electron microscopy images of Ni(O) nanoparticles on GNP (**A**, blue), GNP-O (**B**, orange) and GNP-N (**C**, green) with their corresponding size distributions. **D**) X-ray diffractograms of the same catalysts after passivation in air, thus measuring NiO instead of Ni crystallite sizes. For comparison XRD pattern of the corresponding bare carbon supports are shown as light lines beneath the XRD of each catalyst. The expected peak locations of Ni (circles), NiO (triangles) and Ni_3C (squares) are indicated.

[56], which was not observed for our catalysts (Fig. S9). Thus, XPS analysis of Ni/GNP-O and Ni/GNP catalysts also indicated that the presence of Ni_3C was unlikely. Hence, we prepared nickel on carbon catalysts with different support surface groups, but similar Ni particle sizes and loadings and specific metal surface areas.

3.3. Initial activity

The effect of the catalytic properties of the Ni-based catalysts was investigated under industrially relevant CO_2 hydrogenation pressure and temperatures (30 bar, 300 °C). Fig. 4 shows the CO_2 conversion of the catalysts, which were tested at relatively low conversion (10–20%) to allow examination of their performance far from equilibrium conversion (close to 100% at 30 bar and 300 °C). All bare supports were inactive for CO_2 hydrogenation under these conditions. Ni/GNP-N showed the highest weight based activity, e.g. normalized to Ni content (22.6% CO_2 conversion) (Fig. 4). The initial conversion of Ni/GNP-O and Ni/GNP were 15.6% and 12.9%, respectively. Thus the trend in initial conversion was Ni/GNP-N > Ni/GNP-O > Ni/GNP. This trend was reproducible throughout different catalytic tests and for various batches of catalysts (Fig. S12).

The turnover frequency (TOF) based on this active metal surface area of the fresh catalysts, as determined by H_2 chemisorption, was similar for all catalysts at the start of catalysis (1.3 – 1.6 *10^{-2} s^{-1}, Table 2). Hence the differences in weight-based activity might be explained by a different metal-support interaction and/or specific accessible Ni surface area for the different supports. Alternatively Gonçalves et al. reported for activated carbon and carbon nanotubes [12,40], that the amination treatment increased the catalytic activity during CO_2 hydrogenation, due to enhanced adsorption of CO_2 [23,40,57]. The latter was ascribed to the increased basicity of the support, where the adsorbed reaction intermediates can spill over from the basic groups onto the metal.

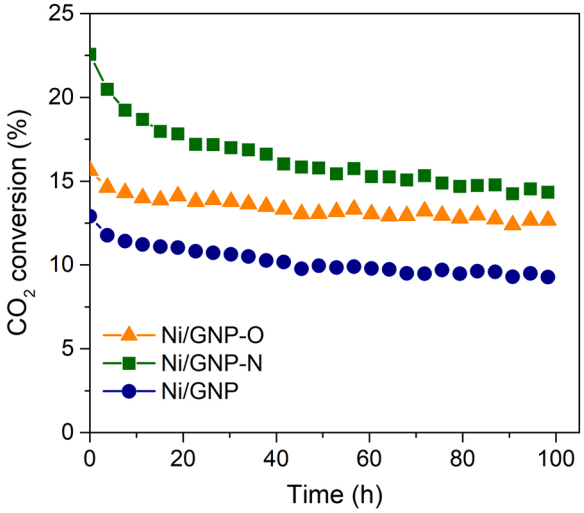

Fig. 4. CO_2 conversion versus time for Ni/GNP (circles, blue), Ni/GNP-O (triangles, orange) and Ni/GNP-N (squares, green). Reaction conditions: 300 °C, 30 bar, 5 mg Ni, GHSV = 7500 mL g_{cat}^{-1} h^{-1}.

3.4. Selectivity

Fig. 5A compares the selectivity towards CH_4 of the Ni catalysts on different supports. Ni/GNP-N gave the highest CH_4 selectivity (initially

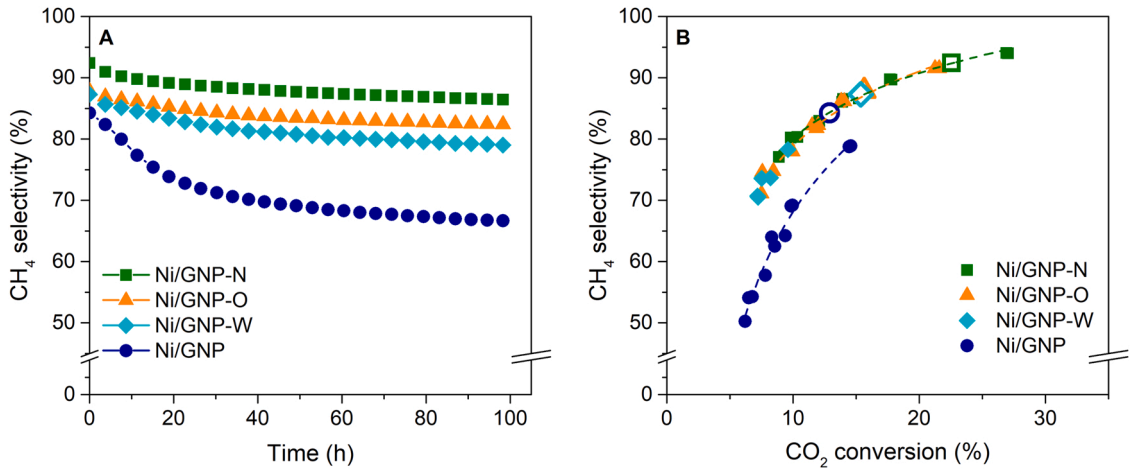

Fig. 5. CH_4 selectivity versus **(A)** time and **(B)** CO_2 conversion of nickel on GNP (circles, blue), GNP-O (triangles, orange) and GNP-N (squares, green) and GNP-W (diamonds, turquoise). Reaction conditions: 300 °C, 30 bar, 5 mg Ni, GHSV = 3750–11250 mL g_{cat}^{-1} h^{-1}.The initial selectivity vs conversion at time = 4 h is shown as open symbols. The dashed lines are a guide for the eye.

92%). The initial selectivity was slightly lower for Ni/GNP-O (86%) and lowest for Ni/GNP (82%). Over the course of 100 h on stream, the CH_4 selectivity of Ni/GNP-O and Ni/GNP-N were relatively stable, while a substantial decrease in selectivity was observed for Ni/GNP (to 65% after 100 h CO_2 hydrogenation). In all cases CO was the main side product.

One must take into account that in the low conversion range the selectivity to CH_4 increases with conversion [45]. After the 100 h stability test, the reactant flow (and as a result GHSV) was changed to vary the CO_2 conversion (Fig. S13). This allowed the study of CH_4 selectivity versus CO_2 conversion (Fig. 5B). Interestingly, the curves for Ni/GNP-N and Ni/GNP-O completely overlap. For Ni/GNP the CH_4 selectivity versus CO_2 conversion was substantially lower than for Ni/GNP-N and Ni/GNP-O. Thus, the support surface treatments have a positive effect on the CH_4 selectivity although it does not seem to matter which kind of surface groups are introduced.

Nanoparticle size and/or the formation of nickel carbide or a carbon layer around the Ni particles might influence the selectivity. However, a slight increase in selectivity is expected for larger particles [45], hence particle size effects cannot explain the differences. Besides, particle growth was severe for Ni/GNP-N, without a great change in selectivity. Similar to the fresh catalysts, XPS showed no indication of the presence of nickel carbide in the used Ni/GNP-O and Ni/GNP (Fig. S9).

For pristine GNP, traces of support with different morphology might have affected the catalysis. Small amounts of, for instance, alkali elements might act as promoter or poison for supported metal catalysts [16, 58–60]. With SEM-EDX analysis, no impurities were detected except some SiO_2 in both GNP and GNP-O (Fig. S5). Because promoters might be active in low concentrations [61], impurities with concentrations below the detection limit of SEM-EDX might still have affected the selectivity. Hence we gave the pristine carbon a mild treatment not to introduce any surface groups, but nevertheless mimicking the treatment for GNP-O and GNP-N by washing in 1 M HNO_3 at room temperature. The surface area of GNP-W was similar to GNP (488 vs 456 m^2 g^{-1} respectively) and the TPD-MS profile was barely affected (Fig. S14). The selectivity of Ni/GNP-W was greatly enhanced as a result of the washing, and now similar to the selectivity of Ni on functionalized carbon (see Fig. 7). At the same time, the washing did not affect the activity as the CO_2 conversion was still similar to the conversion Ni/GNP (Fig. S15). This shows that most likely the CH_4 selectivity is very sensitive to low concentrations of contaminants. The exact influence of small concentrations of contaminants is interesting for further study. In conclusion, support treatment had a positive effect on the CH_4 selectivity, most likely explained by the removal of traces of impurities.

3.5. Stability

The activity evolution, normalized to the activity at $t = 0$, is depicted in Fig. 6A. The activity loss of Ni/GNP-O was 19 ± 5% during 100 h on stream, whereas for Ni/GNP this was 28 ± 5%. The most severe deactivation occurred for Ni/GNP-N, which lost 37 ± 5% activity during 100 h CO_2 hydrogenation under these conditions.

The most likely explanation for the activity loss is the loss of Ni active surface, as TEM analysis after CO_2 hydrogenation (Fig. 6B-D) revealed particle growth in all catalysts. However, the extent of the particle growth was distinctly different for the different catalysts. The least growth occurred for the Ni nanoparticles in the Ni/GNP-O catalysts (from d_s = 5.1 ± 1.2 to 6.0 ± 2.0 nm). This was followed by Ni/GNP (from d_s = 5.3 ± 1.4 to 7.6 ± 2.7 nm) while most severe particle growth had occurred for Ni/GNP-N (from d_s = 5.0 ± 1.7 to 10.7 ± 5.6 nm. This trend was confirmed by XRD (Fig. S16) and H_2 chemisorption (Table 2). Overall the turnover frequencies were quite similar for all three catalysts, both before and after catalysis (Table 2). Although the main peak of the histograms was located around 5–6 nm for all catalysts, the size distributions of Ni/GNP and Ni/GNP-N were more broad than for Ni/GNP-O, especially a longer tail of large particles was visible in the histograms. For Ni/GNP-N, 12% of the nanoparticles counted had a diameter > 10 nm, whereas this value decreased to 5% for Ni/GNP and only 1.4% for Ni/GNP-O. A modest increase of intrinsic activity is expected with increasing particle sizes up to ~8 nm, at least for Ni/GNP-O [45]. However, if there is an optimum above this size, as for example is the case for Co in Fischer Tropsch catalysis [62,63], one would expect the nanoparticles that had grown substantially (> 10 nm) to be less active in catalysis due to the lower surface area.

Fig. 7 shows high resolution STEM images of the catalysts after CO_2 hydrogenation, acquired in both High Angle Annular Dark Field (HAADF-STEM) and integrated differential phase contrast (iDPC) mode. iDPC analysis allows the visibility of the light carbon in the same image as the heavier nickel nanoparticles [64,65], The HAADF-STEM images revealed the appearance of core-shell nanoparticles, with a metallic Ni core surrounded by a 1–2 nm NiO shell, as expected from passivation in air. Some small (<5 nm) nanoparticles were fully oxidized. Especially for GNP-N, the Ni nanoparticles on the edge of the carbon sheets appeared less embedded in the carbon compared to the other supports (Fig. 7E and F). These observations might illustrate a weaker interaction of the nickel metal with specifically the GNP-N support, which has a low density of functional groups and could explain both the initially higher CO_2 conversion and the poorer stability of Ni/GNP-N.

The HAADF-STEM images and the iDPC images of Fig. 7 further

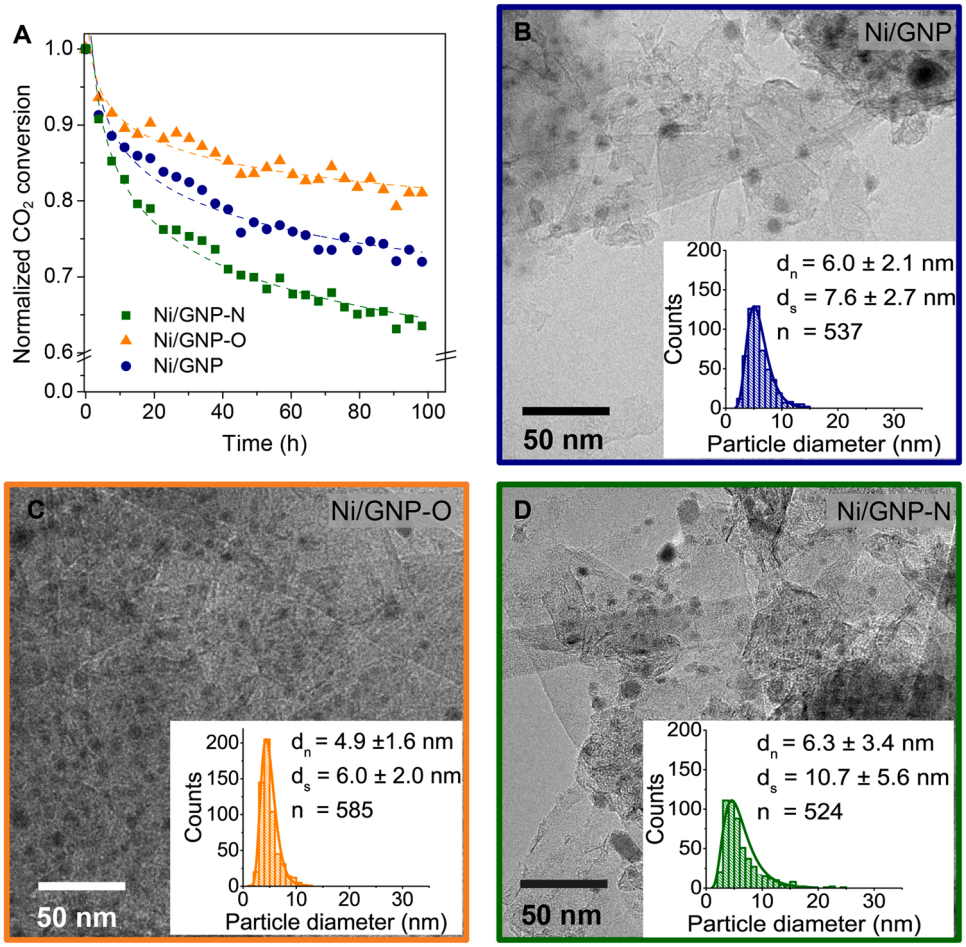

Fig. 6. A) CO_2 conversion normalized to the initial conversion versus time for nickel on GNP (circles, blue), GNP-O (triangles, orange) and GNP-N (squares, green). **(B-C)** Transmission electron microscopy images of Ni(O) nanoparticles on GNP (**B**, blue), GNP-O (**C**, orange) and GNP-N (**D**, green) with their corresponding size distributions after 100 h CO_2 hydrogenation. Reaction conditions: 300 °C, 30 bar, 5 mg Ni, GHSV = 7500 mL g_{cat}^{-1} h^{-1}.

showed that, independent of the support used, several nanoparticles were partially covered by carbon. The combination of the two imaging modes allows identification of these thin carbon layers. Although no statistical information can be derived from the 2D TEM images, we did not observe clear indications that aminated carbon in particular prevented Ni surface coverage as suggested by Wang et al. [21] At the same time, for none of the supports it was observed that these layers of (graphitic) carbon fully covered the nickel surface. This is in line with the accessible metal surface area as measured by H_2 chemisorption as well as the fact that upon exposure to air the nickel nanoparticles were oxidized. The latter would be prevented when they would be fully encapsulated in carbon [66].

Besides particle growth, we checked whether changes in the support might have contributed to the activity loss. The support surface areas remained between 200 and 220 m^2 g_{Ni}^{-1} (Table S3). The D-parameter of both Ni/GNP-O and Ni/GNP was 22 ± 1.0 eV, within error the same as before CO_2 hydrogenation (23 ± 1.0 eV) ((Table S4). Also, the ratio between C−O and C═O surface groups remained the same for both Ni/GNP and Ni/GNP-O (Table S5). Upon heating, the used Ni/GNP-N catalysts still released NO_x in oxygen atmosphere (Fig. S7). Finally, for none of the catalysts, the Ni weight loading was affected (Table 2). This shows that under the catalytic conditions used, the catalyst supports were fairly stable, and there was no significant Ni leaching. At the same time, compared to Ni on oxidic supports [7,67] these catalysts were neither the most stable, nor the most active catalysts for CO_2 hydrogenation. However, it was not our aim to improve existing industrial catalyst but rather to present a series of model catalysts, allowing fundamental studies on support effects. This could be extended to, for instance the addition of another metal, such as Fe [6,40], or metal oxide promoters [35,67–69] improve catalyst activity and/or stability.

All data support the conclusion that the catalyst deactivation was related to a loss of Ni active surface area, due to particle growth, which was influenced by the support properties. Ni/GNP-O was clearly the most stable catalyst, followed by Ni/GNP and finally Ni/GNP-N. It is most likely that the Ni particles remain smallest, and hence the most active in the GNP-O support due the remaining surface groups on this support. The treatment of the carbon to introduce functional groups might also have created defects [38]. However, if these were responsible for anchoring the nanoparticles, these must have been removed during the amination treatment. It is interesting that the interaction of the Ni nanoparticles was stronger with GNP-O than with GNP or GNP-N, despite the fact that nitrogen-containing surface groups are reported to stabilize nanoparticles [21,39,40,70]. Carboxylic surface groups are unstable during the heat treatments and thus are least likely to be present during high pressure CO_2 hydrogenation. Nevertheless, their presence during Ni deposition could have resulted in a higher degree of nanoparticle embedding in the carbon support. Altogether, the support surface groups that are stable up to higher temperatures (> 350 °C), such as anhydrides, phenols, lactones or quinones are most probable to have contributed to the higher stability of the Ni nanoparticles, either by anchoring them, or by blocking their movement over the support.

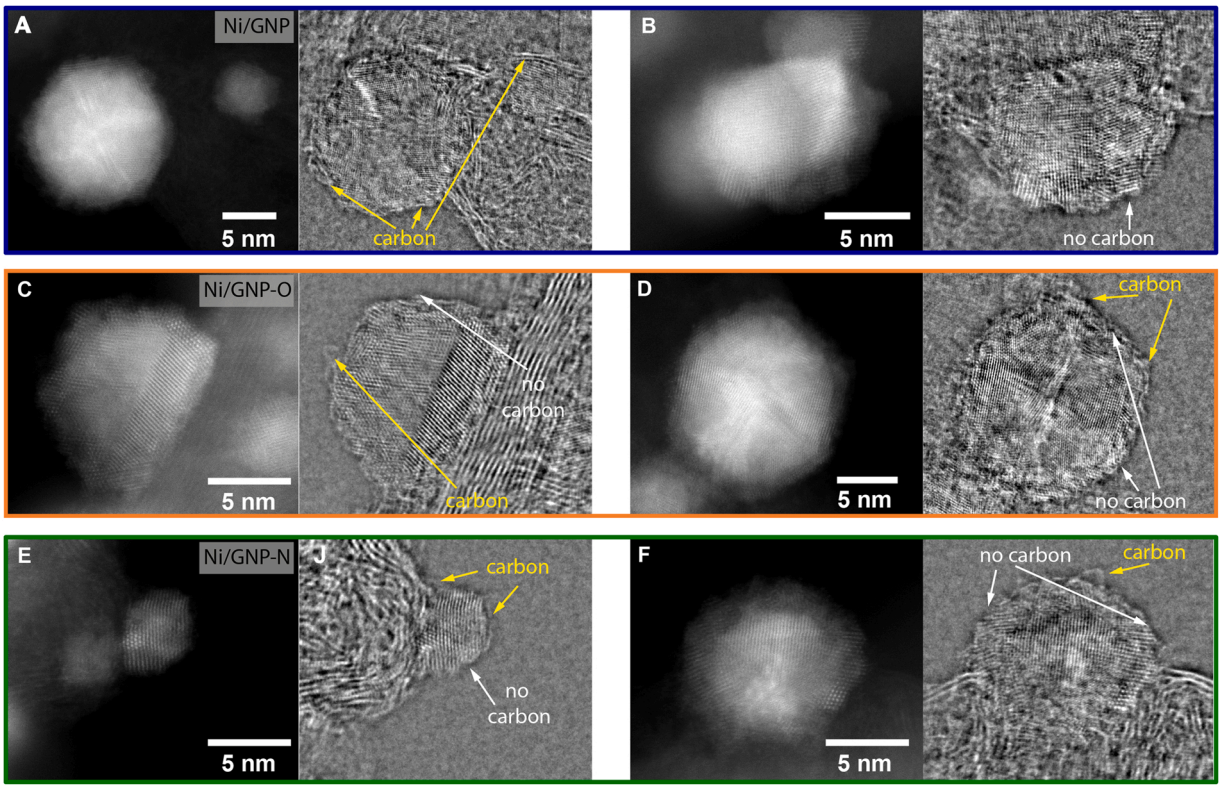

Fig. 7. High resolution electron microscopy images of nickel nanoparticles after catalysis on **(A and B)** GNP and **(C and D)** GNP-O and **(E and F)** GNP-N. For each analyzed location the HAADF-STEM (left) and corresponding iDPC images (right) are shown.

4. Conclusions

We have demonstrated the effect of carbon support functionalization with introduction of both oxygen and nitrogen-containing surface groups for Ni supported catalysts for CO_2 hydrogenation. The surface modifications did not severely affect the Ni nanoparticle size of the fresh catalysts. The treatment to introduce nitrogen-containing surface groups resulted in the initially most active, but also least stable catalyst. Both phenomena were likely caused by the weak interaction between the Ni particles and the support, caused by the low amount of surface groups present. A higher available metal surface area benefited the activity, without affecting the TOF. The introduction of oxygen-containing surface groups significantly enhanced the catalyst stability. The oxygen-containing surface groups that were stable above 350 °C, either anchored the nanoparticles or prevented them from moving over the support. Finally, we showed that the type of support surface groups did not affect the CH_4 selectivity significantly, but it was important to remove trace contaminants. With this work we showed that initial improvement in activity is not always optimal for long term catalysis. When using carbon as a support, the introduction of oxygen-containing support surface groups is advised for the severe conditions needed for synthesis of Ni-based catalysts (at least 350 °C) and high pressure CO_2 hydrogenation.

CRediT authorship contribution statement

Nienke L. Visser: Conceptualization, Methodology, Investigation, Formal analysis, Validation, Writing – original draft, Visualization, Project administration. **Juliette C. Verschoor:** Methodology, Investigation, Formal analysis, Validation. **Luc C.J. Smulders:** Investigation. **Francesco Mattarozzi:** Formal analysis. **David J. Morgan:** Investigation, Formal analysis. **Johannes D. Meeldijk:** Investigation. **Jessi E.S. van der Hoeven:** Supervision. **Joseph A. Stewart:** Conceptualization. **Bart D. Vandegehuchte:** Conceptualization. **Petra E. de Jongh:** Conceptualization, Resources, Supervision, Project administration, Funding acquisition. **All authors:** Writing – review & editing.

Declaration of Competing Interest

The authors declare that they have no known competing financial interests or personal relationships that could have appeared to influence the work reported in this paper.

Data availability

Data will be made available on request.

Acknowledgements

The authors would like to thank Jan Willem de Rijk and Remco Dalebout for their support in the catalytic experiments. Suzan Schoemaker, Kristiaan Helfferich and Laura Barberis are thanked for performing the N_2-physisorption experiments. Dennie Wezendonk is kindly acknowledged for performing the TGA-MS experiments. We thank Ali Kosari for his input on the HRTEM measurements and Claudia Keijzer for performing the SEM measurements. This project is part of the Consortium on Metal Nanocatalysis funded by TotalEnergies OneTech Belgium, under TOTB Contract Ref IPA-5443.

Appendix A. Supporting information

Supplementary data associated with this article can be found in the online version at doi:10.1016/j.cattod.2023.114071.

References

[1] P. Munnik, P.E. De Jongh, K.P.De Jong, Recent developments in the synthesis of supported catalysts, Chem. Rev. 115 (2015) 6687–6718, https://doi.org/10.1021/cr500486u.

[2] B. Miao, S.S.K. Ma, X. Wang, H. Su, S.H. Chan, Catalysis mechanisms of CO_2 and CO methanation, Catal. Sci. Technol. 6 (2016) 4048–4058, https://doi.org/10.1039/c6cy00478d.

[3] T.W. van Deelen, C. Hernández Mejía, K.P. de Jong, Control of metal-support interactions in heterogeneous catalysts to enhance activity and selectivity, Nat. Catal. 2 (2019) 955–970, https://doi.org/10.1038/s41929-019-0364-x.

[4] G. Centi, E.A. Quadrelli, S. Perathoner, Catalysis for CO_2 conversion: a key technology for rapid introduction of renewable energy in the value chain of chemical industries, Energy Environ. Sci. 6 (2013) 1711–1731, https://doi.org/10.1039/c3ee00056g.

[5] A. Jangam, S. Das, N. Dewangan, P. Hongmanorom, W.M. Hui, S. Kawi, Conversion of CO_2 to C1 chemicals: Catalyst design, kinetics and mechanism aspects of the reactions, Catal. Today 358 (2020) 3–29, https://doi.org/10.1016/j.cattod.2019.08.049.

[6] P. Frontera, A. Macario, M. Ferraro, P.L. Antonucci, Supported catalysts for CO_2 methanation: a review, Catalysts 7 (2017) 1–28, https://doi.org/10.3390/catal7020059.

[7] S. Weber, R.T. Zimmermann, J. Bremer, K.L. Abel, D. Poppitz, N. Prinz, J. Ilsemann, S. Wendholt, Q. Yang, R. Pashminehazar, F. Monaco, P. Cloetens, X. Huang, C. Kübel, E. Kondratenko, M. Bauer, M. Bäumer, M. Zobel, R. Gläser, K. Sundmacher, T.L. Sheppard, Digitization in catalysis research: towards a holistic description of a Ni/Al_2O_3 reference catalyst for CO_2 methanation, ChemCatChem 14 (2022), https://doi.org/10.1002/cctc.202101878.

[8] T.A. Le, M.S. Kim, S.H. Lee, T.W. Kim, E.D. Park, CO and CO_2 methanation over supported Ni catalysts, Catal. Today 293 (2017) 89–96, https://doi.org/10.1016/j.cattod.2016.12.036.

[9] L. Shen, J. Xu, M. Zhu, Y.F. Han, Essential role of the support for nickel-based CO_2 methanation catalysts, ACS Catal. 10 (2020) 14581–14591, https://doi.org/10.1021/acscatal.0c03471.

[10] J. Gödde, M. Merko, W. Xia, M. Muhler, Nickel nanoparticles supported on nitrogen–doped carbon nanotubes are a highly active, selective and stable CO_2 methanation catalyst, J. Energy Chem. 54 (2021) 323–331, https://doi.org/10.1016/j.jechem.2020.06.007.

[11] W. Wang, W. Chu, N. Wang, W. Yang, C. Jiang, Mesoporous nickel catalyst supported on multi-walled carbon nanotubes for carbon dioxide methanation, Int. J. Hydrog. Energy 41 (2016) 967–975, https://doi.org/10.1016/j.ijhydene.2015.11.133.

[12] L.P.L. Gonçalves, M. Meledina, A. Meledin, D.Y. Petrovykh, J.P.S. Sousa, O.S.G. P. Soares, Y.V. Kolen'ko, M.F.R. Pereira, Understanding the importance of N−doping for CNT-supported Ni catalysts for CO_2 methanation, Carbon N. Y 195 (2022) 35–43, https://doi.org/10.1016/j.carbon.2022.03.059.

[13] F. Rodríguez-Reinoso, A. Sepúlveda-Escribano, Carbon as catalyst support, Carbon Mater. Catal. (2008) 131–155, https://doi.org/10.1002/9780470403709.ch4.

[14] C. Louis, Z.X. Cheng, M. Che, Characterization of Ni/SiO_2 catalysts during impregnation and further thermal activation treatment leading to metal particles, J. Phys. Chem. 97 (1993) 5703–5712, https://doi.org/10.1021/j100123a040.

[15] J.H. Bitter, M.K. Van Der Lee, A.G.T. Slotboom, A.J. Van Dillen, K.P.De Jong, Synthesis of highly loaded highly dispersed nickel on carbon nanofibers by homogeneous deposition-precipitation, Catal. Lett. 89 (2003) 139–142, https://doi.org/10.1023/A:1024744131630.

[16] D. Beierlein, D. Häussermann, M. Pfeifer, T. Schwarz, K. Stöwe, Y. Traa, E. Klemm, Is the CO_2 methanation on highly loaded $Ni-Al_2O_3$ catalysts really structure-sensitive, Appl. Catal. B Environ. 247 (2019) 200–219, https://doi.org/10.1016/j.apcatb.2018.12.064.

[17] R. Dalebout, L. Barberis, G. Totarella, S.J. Turner, C. La Fontaine, F.M.F. De Groot, X. Carrier, A.M.J. Van Der Eerden, F. Meirer, P.E. De Jongh, Insight into the nature of the ZnO_x promoter during methanol synthesis, ACS Catal. 12 (2022) 6628–6639, https://doi.org/10.1021/acscatal.1c05101.

[18] P. Munnik, M.E.Z. Velthoen, P.E. de Jongh, K.P. de Jong, C.J. Gommes, Nanoparticle growth in supported nickel catalysts during methanation reaction-larger is better, Angew. Chem. 126 (2014) 9647–9651, https://doi.org/10.1002/ange.201404103.

[19] J.R. Rostrup-Nielsen, K. Pedersen, J. Sehested, High temperature methanation: sintering and structure sensitivity, Appl. Catal. A Gen. 330 (2007) 134–138, https://doi.org/10.1016/j.apcata.2007.07.015.

[20] J. Gao, Y. Wang, Y. Ping, D. Hu, G. Xu, F. Gu, F. Su, A thermodynamic analysis of methanation reactions of carbon oxides for the production of synthetic natural gas, RSC Adv. 2 (2012) 2358–2368, https://doi.org/10.1039/c2ra00632d.

[21] W. Wang, C. Duong-Viet, H. Ba, W. Baaziz, G. Tuci, S. Caporali, L. Nguyen-Dinh, O. Ersen, G. Giambastiani, C. Pham-Huu, Nickel nanoparticles decorated nitrogen-doped carbon nanotubes (Ni/N-CNT); a robust catalyst for the efficient and selective CO_2 methanation, ACS Appl. Energy Mater. 2 (2019) 1111–1120, https://doi.org/10.1021/acsaem.8b01681.

[22] J.L. Figueiredo, Functionalization of porous carbons for catalytic applications, J. Mater. Chem. A. 1 (2013) 9351–9364, https://doi.org/10.1039/c3ta10876g.

[23] M.S. Shafeeyan, W.M.A.W. Daud, A. Houshmand, A. Shamiri, A review on surface modification of activated carbon for carbon dioxide adsorption, J. Anal. Appl. Pyrolysis 89 (2010) 143–151, https://doi.org/10.1016/j.jaap.2010.07.006.

[24] T.J. Bandosz, Surface chemistry of carbon materials, Carbon Mater. Catal. (2008) 45–92, https://doi.org/10.1002/9780470403709.ch2.

[25] S. Kundu, Y. Wang, W. Xia, M. Muhler, Thermal stability and reducibility of oxygen-containing functional groups on multiwalled carbon nanotube surfaces: A quantitative high-resolution XPS and TPD/TPR study, J. Phys. Chem. C. 112 (2008) 16869–16878, https://doi.org/10.1021/jp804413a.

[26] J.L. Figueiredo, M.F.R. Pereira, M.M.A. Freitas, J.J.M. Órfão, Modification of the surface chemistry of activated carbons, Carbon N. Y 37 (1999) 1379–1389, https://doi.org/10.1016/S0008-6223(98)00333-9.

[27] M. Führer, T. van Haasterecht, N. Masoud, D.H. Barrett, T. Verhoeven, E. Hensen, M. Tromp, C.B. Rodella, H. Bitter, The synergetic effect of support-oxygen groups and Pt particle size in the oxidation of α-d-glucose: a proximity effect in adsorption, ChemCatChem 14 (2022), https://doi.org/10.1002/cctc.202200493.

[28] J. Zhu, A. Holmen, D. Chen, Carbon nanomaterials in catalysis: proton affinity, chemical and electronic properties, and their catalytic consequences, ChemCatChem 5 (2013) 378–401, https://doi.org/10.1002/cctc.201200471.

[29] M. Park, B.H. Kim, S. Kim, D.S. Han, G. Kim, K.R. Lee, Improved binding between copper and carbon nanotubes in a composite using oxygen-containing functional groups, Carbon N. Y 49 (2011) 811–818, https://doi.org/10.1016/j.carbon.2010.10.019.

[30] R. Beerthuis, J.W. de Rijk, J.M.S. Deeley, G.J. Sunley, K.P. de Jong, P.E. de Jongh, Particle size effects in copper-catalyzed hydrogenation of ethyl acetate, J. Catal. 388 (2020) 30–37, https://doi.org/10.1016/j.jcat.2020.05.006.

[31] C. Prado-Burguete, A. Linares-Solano, F. Rodríguez-Reinoso, C.S.M. de Lecea, The effect of oxygen surface groups of the support on platinum dispersion in Pt/carbon catalysts, J. Catal. 115 (1989) 98–106, https://doi.org/10.1016/0021-9517(89)90010-9.

[32] Dong Jin Suh, P. Tae-Jin, I. Son-Ki, Effect of surface oxygen groups of carbon supports on the characteristics of Pd/C catalysts, Carbon N. Y 31 (1993) 427–435, https://doi.org/10.1016/0008-6223(93)90130-3.

[33] P. Azadi, R. Farnood, E. Meier, Preparation of multiwalled carbon nanotube-supported nickel catalysts using incipient wetness method, J. Phys. Chem. A. 114 (2010) 3962–3968, https://doi.org/10.1021/jp907403b.

[34] B. Fidalgo, L. Zubizarreta, J.M. Bermúdez, A. Arenillas, J.A. Menéndez, Synthesis of carbon-supported nickel catalysts for the dry reforming of CH_4, Fuel Process. Technol. 91 (2010) 765–769, https://doi.org/10.1016/j.fuproc.2010.02.011.

[35] F. Hu, S. Tong, K. Lu, C.M. Chen, F.Y. Su, J. Zhou, Z.H. Lu, X. Wang, G. Feng, R. Zhang, Reduced graphene oxide supported Ni-Ce catalysts for CO_2 methanation: the support and ceria promotion effects, J. CO_2 Util. 34 (2019) 676–687, https://doi.org/10.1016/j.jcou.2019.08.020.

[36] P. Lu, Y. Yang, J. Yao, M. Wang, S. Dipazir, M. Yuan, J. Zhang, X. Wang, Z. Xie, G. Zhang, Facile synthesis of single-nickel-atomic dispersed N-doped carbon framework for efficient electrochemical CO_2 reduction, Appl. Catal. B Environ. 241 (2019) 113–119, https://doi.org/10.1016/j.apcatb.2018.09.025.

[37] T.O. Eschemann, W.S. Lamme, R.L. Manchester, T.E. Parmentier, A. Cognigni, M. Rønning, K.P. De Jong, Effect of support surface treatment on the synthesis, structure, and performance of Co/CNT Fischer-Tropsch catalysts, J. Catal. 328 (2015) 130–138, https://doi.org/10.1016/j.jcat.2014.12.010.

[38] R.M. Malek Abbaslou, A. Tavasoli, A.K. Dalai, Effect of pre-treatment on physico-chemical properties and stability of carbon nanotubes supported iron Fischer-Tropsch catalysts, Appl. Catal. A Gen. 355 (2009) 33–41, https://doi.org/10.1016/j.apcata.2008.11.023.

[39] M.D. Sánchez, P. Chen, T. Reinecke, M. Muhler, W. Xia, The role of oxygen- and nitrogen-containing surface groups on the sintering of iron nanoparticles on carbon nanotubes in different atmospheres, ChemCatChem 4 (2012) 1997–2004, https://doi.org/10.1002/cctc.201200286.

[40] L.P.L. Gonçalves, J.P.S. Sousa, O.S.G.P. Soares, O. Bondarchuk, O.I. Lebedev, Y. V. Kolen'ko, M.F.R. Pereira, The role of surface properties in CO_2 methanation over carbon-supported Ni catalysts and their promotion by Fe, Catal. Sci. Technol. 10 (2020) 7217–7225, https://doi.org/10.1039/d0cy01254h.

[41] D.L. Williamson, C. Herdes, L. Torrente-Murciano, M.D. Jones, D. Mattia, N-Doped Fe@CNT for combined RWGS/FT CO_2 hydrogenation, ACS Sustain. Chem. Eng. 7 (2019) 7395–7402, https://doi.org/10.1021/acssuschemeng.9b00672.

[42] B.H. Arpini, A.H. Braga, L.R. Borges, P. Vidinha, R.V. Gonc, J. Szanyi, L.M. Rossi, Tuning CO_2 hydrogenation selectivity by N-doped carbon coating over nickel nanoparticles supported on SiO_2, ACS Sustain. Chem. Eng. 10 (2022) 2331–2342, https://doi.org/10.1021/acssuschemeng.1c05847.

[43] B. Donoeva, N. Masoud, P.E.De Jongh, Carbon support surface effects in the gold-catalyzed oxidation of 5-hydroxymethylfurfural, ACS Catal. 7 (2017) 4581–4591, https://doi.org/10.1021/acscatal.7b00829.

[44] J.S. Noh, J.A. Schwarz, Estimation of the point of zero charge of simple and mixed oxides by mass titration, J. Colloid Interface Sci. 130 (1989) 157–164, https://doi.org/10.1016/0021-9797(89)90086-6.

[45] N.L. Visser, O. Daoura, P.N. Plessow, J.C.J. Smulders, J.W. de Rijk, J.A. Stewart, B. D. Vandegehuchte, F. Studt, J.E.S. van der Hoeven, P.E. de Jongh, Particle size effects of carbon supported nickel nanoparticles for high pressure CO_2 methanation, ChemCatChem 14 (2022), https://doi.org/10.1002/cctc.202200665.

[46] N. Fairley, V. Fernandez, M. Richard-Plouet, C. Guillot-Deudon, J. Walton, E. Smith, D. Flahaut, M. Greiner, M. Biesinger, S. Tougaard, D. Morgan, J. Baltrusaitis, Systematic and collaborative approach to problem solving using X-ray photoelectron spectroscopy, Appl. Surf. Sci. Adv. 5 (2021), 100112, https://doi.org/10.1016/j.apsadv.2021.100112.

[47] C.O. Ania, J.B. Parra, J.J. Pis, Influence of oxygen-containing functional groups on active carbon adsorption of selected organic compounds, Fuel Process. Technol. 79 (2002) 265–271, https://doi.org/10.1016/S0378-3820(02)00184-4.

[48] C. Moreno-Castilla, M.A. Ferro-García, J.P. Joly, I. Bautista-Toledo, F. Carrasco-Marín, J. Rivera-Utrilla, Activated carbon surface modifications by nitric acid,

hydrogen peroxide, and ammonium peroxydisulfate treatments, Langmuir 11 (1995) 4386–4392.
[49] D.J. Morgan, Comments on the XPS analysis of carbon materials, C 7 (2021) 51, https://doi.org/10.3390/c7030051.
[50] J.C. Lascovich, S. Scaglione, Comparison among XAES, PELS and XPS techniques for evaluation of Sp2 percentage in a-C:H, Appl. Surf. Sci. 78 (1994) 17–23, https://doi.org/10.1016/0169-4332(94)90026-4.
[51] N. Mahata, M.F.R. Pereira, F. Suárez-García, A. Martínez-Alonso, J.M.D. Tascón, J. L. Figueiredo, Tuning of texture and surface chemistry of carbon xerogels, J. Colloid Interface Sci. 324 (2008) 150–155, https://doi.org/10.1016/j.jcis.2008.05.006.
[52] J. Surygała, R. Wandas, E. Śliwka, Oxygen elimination in the process of non-catalytic liquefaction of brown coal, Fuel 72 (1993) 409–411, https://doi.org/10.1016/0016-2361(93)90063-8.
[53] R. Arrigo, M. Hävecker, S. Wrabetz, R. Blume, M. Lerch, J. McGregor, E.P. J. Parrott, J.A. Zeitler, L.F. Gladden, A. Knop-Gericke, R. Schlögl, D.S. Su, Tuning the acid/base properties of nanocarbons by functionalization via amination, J. Am. Chem. Soc. 132 (2010) 9616–9630, https://doi.org/10.1021/ja910169v.
[54] M. Oschatz, J.P. Hofmann, T.W. van Deelen, W.S. Lamme, N.A. Krans, E.J. M. Hensen, K.P. de Jong, Effects of the functionalization of the ordered mesoporous carbon support surface on iron catalysts for the fischer–tropsch synthesis of lower olefins, ChemCatChem 9 (2017) 620–628, https://doi.org/10.1002/cctc.201601228.
[55] D.J. Morgan, Core-level reference spectra for bulk graphitic carbon nitride (g-C3N4), Surf. Sci. Spectra. 28 (2021), 014007. https://doi.org/10.1116/6.0001083.
[56] B.C. Bayer, D.A. Bosworth, F.B. Michaelis, R. Blume, G. Habler, R. Abart, R. S. Weatherup, P.R. Kidambi, J.J. Baumberg, A. Knop-Gericke, R. Schlögl, C. Baehtz, Z.H. Barber, J.C. Meyer, S. Hofmann, In situ observations of phase transitions in metastable nickel (carbide)/carbon nanocomposites, J. Phys. Chem. C. 120 (2016) 22571–22584, https://doi.org/10.1021/acs.jpcc.6b01555.
[57] Q. Pan, J. Peng, T. Sun, S. Wang, S. Wang, Insight into the reaction route of CO_2 methanation: Promotion effect of medium basic sites, Catal. Commun. 45 (2014) 74–78, https://doi.org/10.1016/j.catcom.2013.10.034.
[58] C. Vogt, J. Wijten, C.L. Madeira, O. Kerkenaar, K. Xu, R. Holzinger, M. Monai, B. M. Weckhuysen, Alkali promotion in the formation of CH_4 from CO_2 and renewably produced H_2 over supported Ni catalysts, ChemCatChem 12 (2020) 2792–2800, https://doi.org/10.1002/cctc.202000327.
[59] D. Heyl, U. Rodemerck, U. Bentrup, Mechanistic study of low-temperature CO_2 hydrogenation over modified Rh/Al_2O_3 catalysts, ACS Catal. 6 (2016) 6275–6284, https://doi.org/10.1021/acscatal.6b01295.
[60] A.I. Tsiotsias, N.D. Charisiou, I.V. Yentekakis, M.A. Goula, The role of alkali and alkaline earth metals in the CO_2 methanation reaction and the combined capture and methanation of CO_2, Catalysts 10 (2020) 36, https://doi.org/10.3390/catal10070812.
[61] A. Petala, P. Panagiotopoulou, Methanation of CO_2 over alkali-promoted Ru/TiO_2 catalysts: I. Effect of alkali additives on catalytic activity and selectivity, Appl. Catal. B Environ. 224 (2018) 919–927, https://doi.org/10.1016/j.apcatb.2017.11.048.
[62] G.L. Bezemer, J.H. Bitter, H.P.C.E. Kuipers, H. Oosterbeek, J.E. Holewijn, X. Xu, F. Kapteijn, A.J. Van Diilen, K.P. De Jong, Cobalt particle size effects in the Fischer-Tropsch reaction studied with carbon nanofiber supported catalysts, J. Am. Chem. Soc. 128 (2006) 3956–3964, https://doi.org/10.1021/ja058282w.
[63] J.P. Den Breejen, P.B. Radstake, G.L. Bezemer, J.H. Bitter, V. Frøseth, A. Holmen, K.P.De Jong, On the origin of the cobalt particle size effects in Fischer-Tropsch catalysis, J. Am. Chem. Soc. 131 (2009) 7197–7203, https://doi.org/10.1021/ja901006x.
[64] E. Yücelen, I. Lazić, E.G.T. Bosch, Phase contrast scanning transmission electron microscopy imaging of light and heavy atoms at the limit of contrast and resolution, Sci. Rep. 8 (2018) 1–10, https://doi.org/10.1038/s41598-018-20377-2.
[65] I. Lazić, E.G.T. Bosch, S. Lazar, Phase contrast STEM for thin samples: Integrated differential phase contrast, Ultramicroscopy 160 (2016) 265–280, https://doi.org/10.1016/j.ultramic.2015.10.011.
[66] C. Wang, P. Zhai, Z. Zhang, Y. Zhou, J. Zhang, H. Zhang, Z. Shi, R.P.S. Han, F. Huang, D. Ma, Nickel catalyst stabilization via graphene encapsulation for enhanced methanation reaction, J. Catal. 334 (2016) 42–51, https://doi.org/10.1016/j.jcat.2015.10.004.
[67] W.L. Vrijburg, G. Garbarino, W. Chen, A. Parastaev, A. Longo, E.A. Pidko, E.J. M. Hensen, Ni-Mn catalysts on silica-modified alumina for CO_2 methanation, J. Catal. 382 (2020) 358–371, https://doi.org/10.1016/j.jcat.2019.12.026.
[68] R. Dalebout, L. Barberis, N.L. Visser, J.E.S. van der Hoeven, A.M.J. van der Eerden, J.A. Stewart, F. Meirer, K.P. de Jong, P.E. de Jongh, Manganese oxide as a promoter for copper catalysts in CO_2 and CO hydrogenation, ChemCatChem 14 (2022) 1–13, https://doi.org/10.1002/cctc.202200451.
[69] R. Beerthuis, N.L. Visser, J.E.S. van der Hoeven, P. Ngene, J.M.S. Deeley, G. J. Sunley, K.P. de Jong, P.E. de Jongh, Manganese oxide promoter effects in the copper-catalyzed hydrogenation of ethyl acetate, J. Catal. 394 (2021) 307–315, https://doi.org/10.1016/j.jcat.2020.11.003.
[70] R. Shi, J. Zhao, S. Liu, W. Sun, H. Li, P. Hao, Z. Li, J. Ren, Nitrogen-doped graphene supported copper catalysts for methanol oxidative carbonylation: Enhancement of catalytic activity and stability by nitrogen species, Carbon N. Y 130 (2018) 185–195, https://doi.org/10.1016/j.carbon.2018.01.011.